

Article

A Multi-Scale Study on the Property Degradation of High-Temperature Treated Beishan Granite

Xiang Zhang, Manke Wei *, Zhen Lei and Ying Chen

School of Architecture and Planning, Yunnan University, Kunming 650091, China

* Correspondence: weimanke@mail.ynu.edu.cn

Abstract: Granite is the main host rock for the underground storage of nuclear waste in Beishan, China. Heat is continuously generated during the long-term disposal of nuclear waste; therefore, it is important to investigate the influence of high temperature on the physical and mechanical properties and the constitutive relation of Beishan granite. In this study, laboratory experiments on heat-treated (25 °C, 200 °C, 400 °C, 600 °C and 800 °C) Beishan granite samples were performed in combination with nuclear magnetic resonance (NMR) analysis and regular physical-mechanical tests. The results show that the elastic modulus tends to decline faster at the temperature ranges of 25–200 °C and 600–800 °C by approximately 26.767% and 66.996%, respectively. Compared with the results at 25 °C, the peak stress decreases by 72.664% at 800 °C. The peak strain increases gradually from 25 °C to 600 °C and abruptly from 600 °C to 800 °C. The peak strain at 800 °C is 2.303× greater than that at 25 °C. Based on the damage theory, the Weibull distribution, the rock damage threshold point, and the residual strength, this study corrected the Drucker–Prager (D–P) criterion to consider the damage stress and then to establish the constitutive model of thermally damaged Beishan granite. The parameters required for the model are conventional mechanical parameters that can be calculated from the uniaxial test results, thus making the model convenient to apply. Meanwhile, the mechanical behavior of thermally damaged Beishan granite under uniaxial compression was simulated using the Particle Flow Code (PFC) to explore the development of cracks from the microscopic scale. The research results can provide theoretical support for the calculation and numerical simulation related to the mechanics of high-temperature treated rocks.



Citation: Zhang, X.; Wei, M.; Lei, Z.; Chen, Y. A Multi-Scale Study on the Property Degradation of High-Temperature Treated Beishan Granite. *Minerals* **2022**, *13*, 27.

<https://doi.org/10.3390/min13010027>

Academic Editor: Mamadou Fall

Received: 16 November 2022

Revised: 10 December 2022

Accepted: 21 December 2022

Published: 23 December 2022



Copyright: © 2022 by the authors. Licensee MDPI, Basel, Switzerland. This article is an open access article distributed under the terms and conditions of the Creative Commons Attribution (CC BY) license (<https://creativecommons.org/licenses/by/4.0/>).

Keywords: Beishan granite; constitutive model; high-temperature; thermal damage; PFC

1. Introduction

The long-term safe disposal of high-level radioactive waste is a major issue for the sustainable development of nuclear energy and environmental protection [1]. Currently, deep geological disposal is considered to be one of the best options for the storage of high-level radioactive waste [2]. The preferential host rocks include salt beds [3,4], shale [5,6] and granite [7,8]. Because of its good integrity, homogeneity, and low porosity and permeability [9–11], the host rock formation of granite has been used in many countries [12], such as the crystalline Archean granite–gneisses at Yeniseisky in Russia [13], the granite formation at the Grimsel test site in Switzerland [14], and the Lac du Bonnet granite formation in southeastern Manitoba in Canada [15]. In recent years, the Chinese nuclear power industry has developed rapidly. According to the data of the World Nuclear Association, as of July 2022, China has 20 nuclear reactors under construction, with the largest net capacity in the world [16]. A deep granite formation located in the Beishan region of Gansu Province in China is currently considered the preferred site for the geological storage of high-level radioactive waste [17]. Nuclear waste will continue to release heat during disposal, and the duration of the nuclear heat pulse is 10^3 to 10^4 years [18]. Due to the complexity of the mineral composition of granite and the different coefficients of thermal expansion, the mineral expansion that occurs at a high temperature can exert significant thermal stresses

between minerals, resulting in the formation of microcracks and fractures in rock [19,20]. This effect will significantly influence the mechanical properties of rock, including its elastic modulus, peak stress, and peak strain [21], which will in turn affect the long-term safety and stability of the repository. Therefore, thermal damage to granite is a key scientific research issue in the construction and development of nuclear waste underground repositories.

To date, researchers have investigated the physical and mechanical properties of heat-treated granite using a variety of experimental and numerical methods. Zhao et al. [22] studied the thermal conductivity of heat-damaged Beishan granite under uniaxial compression with the transient plane source method using a servo-controlled compression machine and an acoustic emission (AE) monitoring system. Their results show that with increasing temperature, the cumulative AE hits of the specimens at the crack damage stress and the peak stress increase nonlinearly, the initial and peak lateral thermal conductivities of the specimens decrease, and their differences increase. In addition, the high-temperature treated specimens experienced greater shrinkage deformation to reach the peak thermal conductivity. Chen et al. [23] used high-temperature uniaxial compression and a three-point bending method to determine the macroscopic mechanical properties of Fujian granite and performed scanning electron microscopy (SEM) and optical microscopy to study the microstructure of the damaged samples. The results show that the uniaxial compressive strength, Young's modulus, and fracture toughness of granite decrease with increasing temperature. In addition, the connection between minerals becomes weaker, and the main failure mode is intergranular cracking when the temperature is below 800 °C and transgranular cracking when the temperature is close to 1000 °C. Gautam et al. [24] experimentally investigated the effect of temperature on the physical and mechanical properties of Jalore granite in India using SEM. The results show that thermogenic cracks have a long densification phase and exhibit a rapid increase in crack density due to the complexity of their thermal expansion rate, with the expansion of quartz as the most significant effect. The compressive and tensile strengths increase gradually for temperatures below 300 °C and decrease sharply above 300 °C. In the range of 300–600 °C, the stress–strain curves exhibit plastic behavior, reflecting the brittle-tough transition. Tomas et al. [25] performed physical and mechanical tests on granite specimens from northern Portugal and compared the results with a large number of published case studies, showing that the variations in porosity, unit weight, ultrasonic wave velocity, elastic modulus, and uniaxial compressive stress are mainly related to the induced thermal stress from the anisotropic thermal expansion of mineral particles. Wu et al. [26] used uniaxial compression tests, ultrasonic velocity analysis, AE monitoring, and SEM to study the effect of thermal damage at different temperatures on the physical and mechanical properties of Beishan granite, and the results show that the peak strength, P-wave velocity, and mass loss rate decreased sharply with increasing temperature. Cracks increased and gradually formed fracture zones that eventually lead to the destruction of the sample.

The constitutive model is mainly used to study the relationship between stress and strain. Based on the Weibull distribution and Lemaitre strain equivalence principle, Xu et al. [27] used the Drucker–Prager (D–P) criterion and analyzed thermal damage at high temperature and mechanical damage at high pressure, proposed nonlinear coupled total damage parameters, and then established a thermomechanical coupled damage model of granite. The theoretical results obtained using the model are in good agreement with the experimental values. Liu et al. [28] used the D–P criterion and the Weibull distribution to develop a statistical constitutive model of high-temperature granite that considered the damage threshold, the residual stress, and the thermal damage. This model enables the evaluation of the rock toughness and brittleness based on the damage evolution and analyzes the effect of the Weibull parameter and temperature on the damage evolution. Wang et al. [29] derived the temperature dependence based on the variations in the parameters such as the tensile strength, Young's modulus, Poisson's ratio, and coefficient of thermal expansion of granite at 1000 °C and then combined it with the constitutive model based on the classical Mohr–Coulomb model with strain softening and tension cutoff. Then,

a new constitutive law was verified by performing a uniaxial compression test. Wang et al. [30] combined the 3D D–P criterion, the compaction coefficient, the damage variable correction factor, and the thermal damage variable to establish a new whole-process thermomechanical constitutive model considering the rock strain softening caused by the compaction stage and thermal shock in the uniaxial compression test. The model can be used to estimate the overall evolution of rock damage after high-temperature treatment. Xie et al. [31] determined the yield point based on the stress difference method, modified the Weibull distribution, and proposed a piecewise constitutive model bounded by the yield point, which could reflect the complete stress-strain curves of the rock.

For the microstructure and microcracks of thermally damaged granite, Zhao et al. [32] used the mercury intrusion technique to study the pore characteristics of granite under different thermal cycling conditions. The results show that the number of thermal cycles has little effect on the pore structure, while the temperature has a greater effect, and decreases the complexity of the pore structure for pores with sizes from 0.01 to 10 μm and increases the complexity of pores with sizes from 10 to 200 μm . Miao et al. [33] combined AE, digital image correlation, and optical microscopic observations to reveal the key mechanism of the mechanical and fracture behavior of heat-treated Beishan granite. Li et al. [34] investigated the effect of cyclic heating and cooling on the pore structure of granite by performing nuclear magnetic resonance (NMR) and magnetic resonance imaging (MRI). The results show that the porosity increases significantly and the ultrasonic velocity decreases sharply after cyclic heating and cooling. It was confirmed by MRI observations that the expansion and deepening of microcracks in granite during thermal cycling were due to the combined effects of the inhomogeneous expansion and contraction of particles, the transformation of mineral crystal structure, the fatigue damage, and the thermal shock caused by cooling. Wang F et al. [35] investigated the effect of low and high heating rates on the thermal cracking of granite using a continuous medium-based numerical method. The results show that at a low heating rate, the thermal stress variation is mainly controlled by the coefficient of nonhomogeneous thermal expansion of the mineral grains. At a high heating rate, larger cracks and newly induced microcracks form due to a wider range of concentrated tensile stresses. Different heating rates induce different cracking behaviors, affecting the strength and final damage form of the granite. Liu et al. [36] performed discrete element modeling of mineral structures to study the stress–strain, AE, and crystal-scale crack extension patterns of inhomogeneous rocks. Based on the effective medium theory, Xie et al. [37] proposed an exponential model to describe the influence of the crack closure effect on the constitutive relation, which was verified by the uniaxial compression test. The results show that the microcrack volume ratio is positively correlated with the crack density parameters, and the material damage caused by microcrack can be identified and quantified by it.

This work is a multi-scale study that combines the theoretical study, the physical-mechanical tests, and the numerical simulation to investigate the degradation effect of high temperature on granite properties. Heat treatment, NMR, physical, and mechanical experiments were carried out. Based on the Lemaitre strain equivalence principle and the D–P criterion, the Weibull distribution was introduced to describe the microelement strength distribution of rock and to build the constitutive and high-temperature thermal damage constitutive laws of Beishan granite. The parameters required for the damage constitutive model are conventional mechanical parameters that can be calculated from the uniaxial test results, thus making the model convenient to apply. The model can reflect the stress-strain relationship of high-temperature treated granite. The simulation of the uniaxial compression mechanical behavior of heat-treated granite was completed by using PFC, and the fracture mechanism was revealed from the perspective of micro-crack development. The research results can provide theoretical support for the calculation and numerical simulation related to the mechanics of high-temperature treated rocks.

2. Experiments

This section is about the high-temperature treatment test, and the physical and mechanical properties tests on Beishan granite.

2.1. Beishan Granite Sample

The samples were obtained from the granite stratum in the preselection area of Beishan, Gansu. The cores were drilled horizontally from the wall of the tunnel after excavation at the pit exploration facility. The core is granitic in structure and is light gray with black spots, and the main minerals include plagioclase, alkali feldspar, quartz, and black mica. The mineral composition was obtained by X-ray diffraction analysis (SmartLab, Rigaku, Japan) as 67.90% feldspar, 27.40% quartz, and 4.70% mica. The preparation method and processing accuracy met the relevant standards. The specimens of $\varphi 50 \text{ mm} \times 25 \text{ mm}$ and $\varphi 50 \text{ mm} \times 100 \text{ mm}$ were made and treated at different temperature levels for the uniaxial compression test and Brazilian splitting test, respectively, as shown Figure 1.

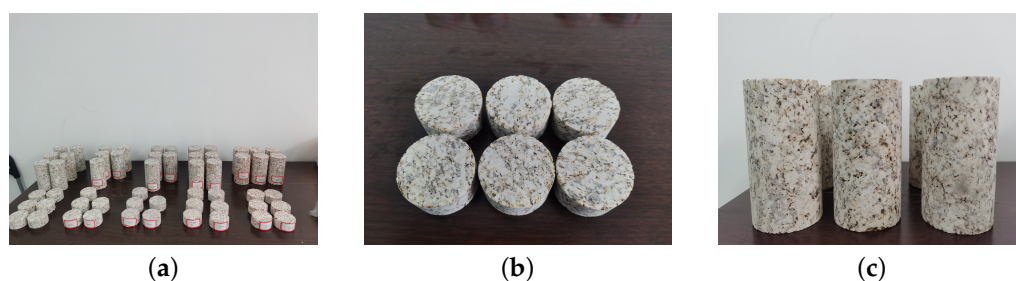


Figure 1. Beishan granite specimens. (a) Beishan granite specimens; (b) $\varphi 50 \text{ mm} \times 25 \text{ mm}$; (c) $\varphi 50 \text{ mm} \times 100 \text{ mm}$.

2.2. Experimental Studies

2.2.1. High-Temperature Treatment Test

A KSL-1200X muffle furnace (maximum temperature of $1200 \text{ }^{\circ}\text{C}$, heating rate $\leq 10 \text{ }^{\circ}\text{C}/\text{min}$, temperature control accuracy $\pm 1 \text{ }^{\circ}\text{C}$, HF-Kejing, Hefei, China) was used for the high-temperature treatment at $25 \text{ }^{\circ}\text{C}$, $200 \text{ }^{\circ}\text{C}$, $400 \text{ }^{\circ}\text{C}$, $600 \text{ }^{\circ}\text{C}$ and $800 \text{ }^{\circ}\text{C}$ for a total of five test groups. The experimental work of Chen [38] has indicated that $5 \text{ }^{\circ}\text{C}/\text{min}$ is usually the threshold of the heating rate; above this threshold the damage mechanism of granite changes. To avoid thermal shock to the specimens, this study fixed a heating rate of $4 \text{ }^{\circ}\text{C}/\text{min}$. The preset temperature of the muffle furnace was maintained for 1h to allow the rock specimen to be fully heated. When the heating process was completed, the specimen naturally cooled to room temperature before being removed. As shown in Figure 2, with increasing temperature, the specimens gradually became more reddish brown and was more susceptible to damage with smaller forces, and the specimens of the $800 \text{ }^{\circ}\text{C}$ test group made a sharp sound after a slight collision.



Figure 2. Heat-treated granite specimens.

2.2.2. Physical Property Tests

Electronic scales, Vernier calipers, and wave velocity testers (RSM-SY5(T), SINOROCK, Wuhan, China) were used to measure the variations in mass, volume, density, and wave velocity of the heat-treated specimens.

Figure 3 shows the relationship of some physical properties with increasing temperature. The mass, density, and wave velocity of the specimens gradually decrease with increasing temperature, while the volume shows the opposite trend, and all four parameters subsequently vary. In particular, the mass of the specimen decreased by 0.116% and 0.118% at the temperature intervals of 25 °C to 200 °C and 400 °C to 600 °C, respectively, showing faster change compared with the result obtained at 25 °C. The former decrease is due to the evaporation of free and bound water inside the specimens during the heating process. In the latter temperature interval, particularly between 300 °C and 500 °C, the contents of quartz, feldspar, hornblende, and mica fluctuate with increasing temperature, indicating that heating promotes physical and chemical reactions in granite components [39]. Meanwhile, the volume, density, and wave velocity change significantly after 400 °C, and a change-rate inflection point is present between 400 and 600 °C. It indicates that with increasing temperature, particularly above 400 °C, the internal physicochemical reaction of granite is more intense, and the degree of thermal damage is more important.

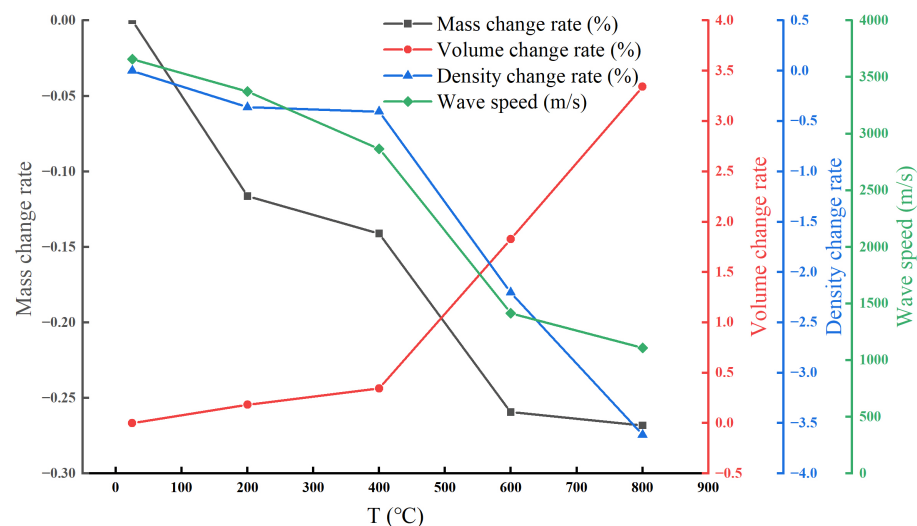


Figure 3. Effect of heat treatment on the physical properties of Beishan granite.

A MesoMR23-060H-I NMR analyzer (magnetic field strength of 0.52 ± 0.05 T, magnetic field stability of ≤ 300 Hz/h, maximum sampling width/kHz of 2000 kHz, Niumai, Suzhou, China) was used to perform NMR experiments on heat-treated specimens, and the pore size distribution characteristics were analyzed by T_2 spectroscopy (MesoMR23-060H-I, Niumai, Suzhou, China) to reveal the development of microcracks.

NMR was used to detect the relaxation response of 1H protons in rock samples by performing Carr–Purcell–Meiboom–Gil pulse sequence tests on fully saturated rock specimens to obtain the transverse relaxation time T_2 [40]. T_2 is mainly influenced by the ratio of the surface area to the volume of the pores, which is proportional to the pore radius. Therefore, the pore size distribution of rock can be characterized by the NMR signal intensity of the T_2 curve (amplitude, peak area, and continuity) [41]. Figure 4 shows the T_2 profiles of the specimens obtained after different temperature treatments. The distribution characteristics of the microcrack of the specimens can be analyzed according to the T_2 spectrum amplitude. The T_2 amplitudes show a double-peak feature. The left peak corresponds to the fine pores, and the right peak corresponds to the microcracks. The left peak is lower than the right peak.

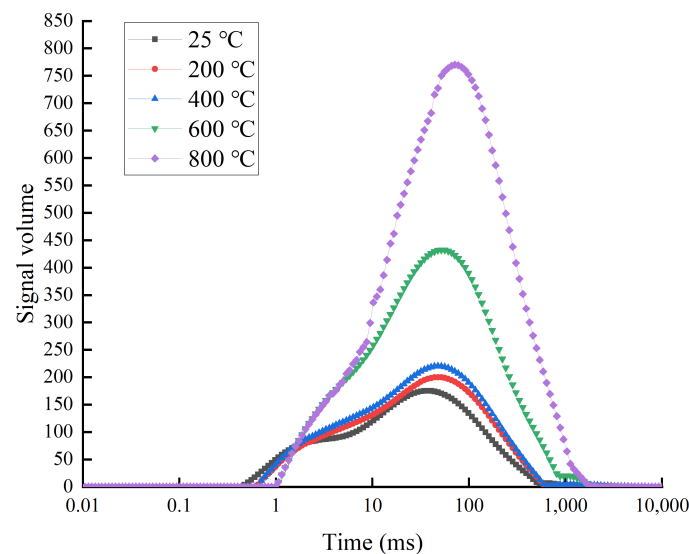


Figure 4. T_2 spectra from NMR on heat-treated Beishan granite.

Overall, the high temperature has a significant effect on the T_2 values of the Beishan granite. In the range of 25–400 °C, there is no significant difference in the left peak T_2 amplitude with increasing temperature, and the right peak T_2 amplitude increases slightly, indicating that there is no significant expansion of granite pores in this temperature range. In the range of 400–800 °C, the left peak T_2 amplitude increases with increasing temperature, and the right peak and the corresponding area under the curve increase significantly. Based on the observation of the microstructure, Sun Z et al. [42] found that boundary cracks were generated between feldspar crystals and between feldspar grains and quartz grains at 500 °C. At 600 °C, the quartz α/β phase transition point was exceeded, and large transparent transgranular cracks were generated in quartz particles, accompanied by an obvious transgranular network. These results show that a high temperature leads to the phase transformation of quartz, the considerable development of internal cracks, and increases in the size and volume of the pores. A large number of microcracks develop as new pores are formed.

Figure 5 shows the MRI results from NMR on the specimens of 25 °C, 200 °C and 600 °C. Figure 5d shows the relative intensity range of 1H in the internal pores, and the red color shows the stronger 1H signal that indicates greater fluid intrusion into the specimen and greater crack development. In the image, the black part is the imaging background, and the middle-colored part is the proton density-weighted image.

It can be deduced from the NMR images that the proton density distribution is uniform at 25 °C, and there is no obvious concentration of proton density, indicating that the specimen is mainly dominated by fine pores at this temperature. With increasing temperature, the rock specimen undergoes more thermal damage, the proton density exhibits a more clustered distribution, the microcracks gradually initiate, develop and expand, and the volume gradually increases. There is a distribution of high-proton-density (red) regions at 600 °C. Meanwhile, green pixel clusters are commonly produced by the aggregation of microcrack interactions, indicating that the crack development of Beishan granite is particularly pronounced at this temperature. The T_2 pattern and imaging analysis show that with increasing temperature, the moisture inside the specimen evaporates through the microcracks, and the resulting pressure leads to a slight expansion of the cracks. When the temperature exceeds the phase change point of quartz, the temperature gives rise to cracks through the crystal as well as microcrack expansion between the grains and more mineral physicochemical reactions. The fine cracks inside the specimen gradually develop to form a larger connected area and agglomerate into a crack network, leading to the further deterioration of the physical properties of the rock.

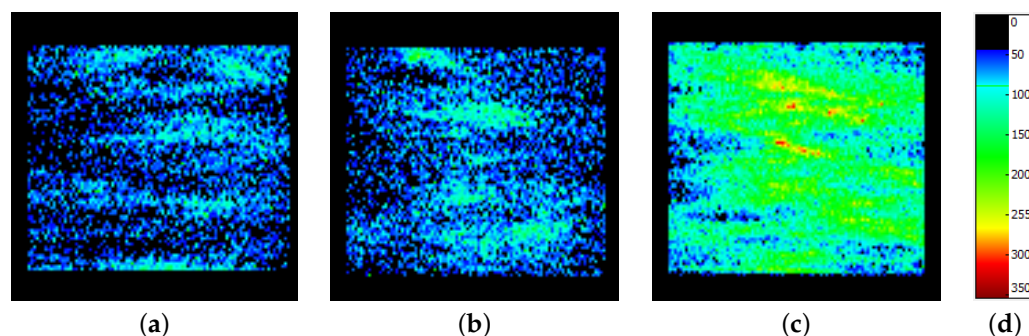


Figure 5. MRI of heat-treated Beishan granite. (a) 25 °C (b) 200 °C (c) 600 °C (d) legend.

2.2.3. Mechanical Property Tests

The uniaxial compression test (φ 50 mm \times 25 mm) and Brazilian splitting test (φ 50 mm \times 100 mm) were conducted on the heat-treated rock samples using a HUT305A type 300 kN microcomputer-controlled electrohydraulic servo universal testing machine (as shown in Figure 6, WANCE, Shenzhen, China) to study the effect of high temperature on the mechanical properties of rock.



Figure 6. HUT305A type 300 kN microcomputer-controlled electrohydraulic servo universal testing machine.

Figure 7 shows the damage modes of rock after different temperature treatments. With increasing temperature, the damage at the peak strength increased, and the specimens were gradually powdered. In the Brazilian splitting test, when the stress reached the peak strength, a primary fracture expanded along the loading direction, and with increasing temperature, more secondary cracks were produced around the primary fracture, with a denser distribution.

Figure 8 shows the results of the mechanical tests. In the uniaxial compression test, with the increase in temperature, the peak of the stress–strain curve decreases significantly and gradually levels off. The modulus of elasticity and the peak stress gradually decreases, and the peak strain shows an overall gradual increasing trend. In particular, the elastic modulus tends to decline faster at the temperature ranges of 25–200 °C and 600–800 °C by approximately 26.767% and 66.996%, respectively. The former is due to the evaporation of water vapor that leads to a slight expansion of the microcracks. The latter is due to the thermal stress generated by the thermal expansion between the grains, leading to the rapid expansion of the crack and the rapid deterioration of mechanical properties. Comparing with the results at 25 °C, the peak stress decreases by 72.664% at 800 °C. The peak strain increases gradually from 25 °C to 600 °C and abruptly from 600 °C to 800 °C. The peak strain at 800 °C is 2.303 \times greater than that at 25 °C. This indicates that the granite gradually changes from brittle to ductile after reaching a certain temperature. It has been shown that the temperature range from 400 °C to 600 °C can be considered the critical temperature range for the brittle-to-ductile transition [43].

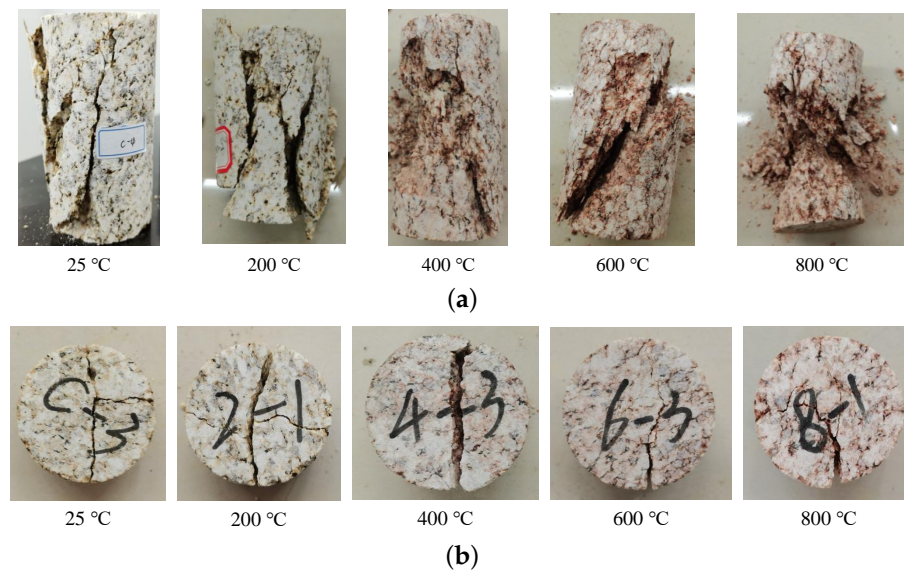


Figure 7. Specimens after damage by uniaxial compression and Brazilian splitting tests. (a) Uniaxial compression test; (b) Brazilian splitting test.

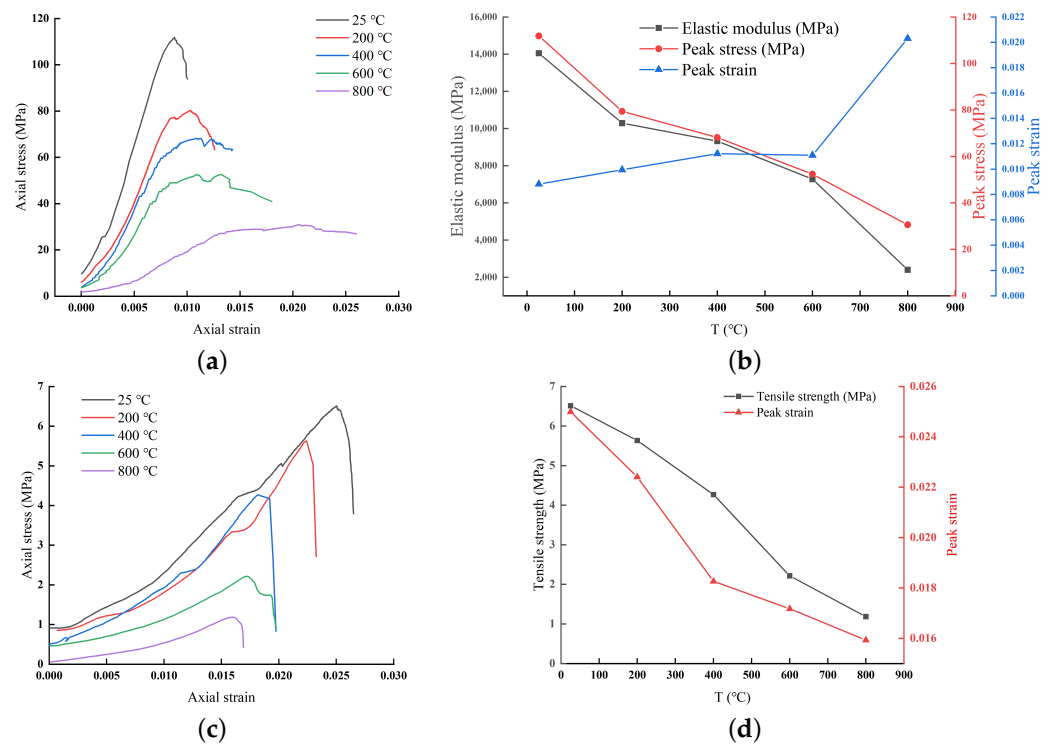


Figure 8. Effect of temperature on the mechanical properties of Beishan granite. (a) Uniaxial compression test: stress–strain curve; (b) Uniaxial compression test: mechanical properties; (c) Brazilian splitting test: stress–strain curve; (d) Brazilian splitting test: mechanical properties.

3. Constitutive Model

Based on the results of uniaxial compression tests, this section introduces the establishment of the damage constitutive model under normal temperature loading and the deduction of the high-temperature damage constitutive model. The proposed mechanical model consists of a Kelvin body and a damaged body in parallel, and the D–P criterion is modified.

3.1. Damage Constitutive Model under Normal Temperature Loading

Many natural pores and tectonic fractures are distributed inside rock; they develop under loading and increasing temperature and eventually cause damage and failure. Among various mechanical components, the Calvin body can be used to characterize the viscoelastic properties of materials [44], and can be used to establish constitutive models for the mechanical response of materials such as rocks. However, since such models do not include damage properties to consider the influence of thermal damage of granite, this paper assumes that the mechanical model of granite consists of a Calvin body and a damaged body in parallel, as shown in Figure 9.

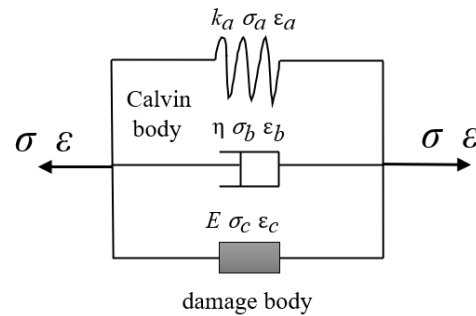


Figure 9. Damage intrinsic mechanics model.

According to the damage theory proposed by Liu et al. [45], assuming that the number of microelements contained inside the granite is N , the number of microelements completely destroyed inside the rock due to external loading is n , and the damage variable is denoted by D . Then, the damage variable D_σ caused by the loading is given by:

$$D_\sigma = \frac{n}{N}. \tag{1}$$

Considering that the rock microelement strength obeys the Weibull distribution [46], the microelement strength probability density function $f(x)$ of granite can be computed as:

$$f(x) = \begin{cases} 0, & x \geq 0 \\ \frac{m}{K} \left(\frac{x}{K}\right)^{m-1} \exp\left[-\left(\frac{x}{K}\right)^m\right], & x < 0. \end{cases} \tag{2}$$

The distribution function $F(x)$ is obtained as:

$$F(x) = 1 - \exp\left[-\left(\frac{x}{K}\right)^m\right], \tag{3}$$

where x is a Weibull distributed random variable and m and K are parameters in the Weibull distribution that represent the shape parameter and the size parameter, respectively.

A threshold exists in the process of deformation and damage. When the stress is lower than the threshold, no damage occurs [47]. When the external load exceeds the threshold and reaches a certain value, the number of microelements that undergo damage inside the rock can be expressed as:

$$n = N \int_0^x f(\sigma) d\sigma. \tag{4}$$

Combining Equation (3) and substituting Equation (4) into Equation (1), the following equation is obtained:

$$D_\sigma = \frac{n}{N} = \frac{N \int_0^x f(\sigma) d\sigma}{N} = \int_0^x f(\sigma) d\sigma = 1 - \exp\left[-\left(\frac{f(\sigma)}{K}\right)^m\right]. \tag{5}$$

Using the D–P criterion to measure the strength of the rock microelement, we obtain:

$$f(\sigma) = \alpha I_1 + \sqrt{J_2}, \tag{6}$$

where $\alpha = \frac{\sin \varphi}{\sqrt{9+3(\sin \varphi)^2}}$, φ is the angle of internal friction, and I_1 is the first invariant of the stress tensor and J_2 is the second invariant of the deviatoric stress tensor that are expressed as:

$$\begin{cases} I_1 = \sigma_1^* + \sigma_2^* + \sigma_3^*, \\ J_2 = \frac{1}{6} [(\sigma_1^* - \sigma_2^*)^2 + (\sigma_2^* - \sigma_3^*)^2 + (\sigma_3^* - \sigma_1^*)^2]. \end{cases} \tag{7}$$

Although the D–P criterion is widely used, it is used as an ideal elastic–plastic criterion that assumes that damage occurs when the rock is subjected to a certain load. Since there exists a threshold for rock damage, its influence needs to be considered. Therefore, the microelement intensity can be corrected as follows:

$$f(\sigma)' = f(\sigma) - C, \tag{8}$$

where C is the strength at the threshold (threshold strength), and its corresponding strain is the threshold strain ε_c . The threshold stress $C = 40\% \sigma_D$ (σ_D is the peak strength) was set according to the experimental study of Martin et al. [48] on Lac du Bonnet granite.

When the load is less than C , no damage or very little damage occurs, and its damage variable can be considered as 0 [49]. Equation (8) can then be substituted into Equation (6) to obtain the expression for the load-related damage variable.

$$D_\sigma = \begin{cases} 0, & \varepsilon < \varepsilon_c, \\ 1 - \exp \left[- \left(\frac{\alpha I_1 + \sqrt{J_2} - C}{K} \right)^m \right], & \varepsilon \geq \varepsilon_c. \end{cases} \tag{9}$$

Based on the relationship between the nominal stress σ_i and the effective stress σ_i^* in the strain equivalence assumption proposed by Lemaitre et al. [50], the following equation is obtained:

$$\sigma_i = \sigma_i^* (1 - D), i = 1, 2, 3 \tag{10}$$

In addition, the rock will possess a certain residual strength after damage. Considering this, the damage variable correction factor β [51] in Equation (10) is introduced as:

$$\sigma_i = \sigma_i^* (1 - \beta D), i = 1, 2, 3, \tag{11}$$

where $\beta = \sqrt{\frac{\sigma_r}{\sigma_D}}$, and σ_r is the residual strength.

When the rock is in the elastic phase, it obeys Hooke’s law:

$$\varepsilon_1 = \frac{1}{E} [\sigma_1^* - \nu(\sigma_2^* + \sigma_3^*)], \tag{12}$$

where E is the modulus of elasticity and ν is the Poisson ratio.

Substitution of Equation (11) into Equation (12) yields:

$$\varepsilon_1 = \frac{1}{E(1 - \beta D)} [\sigma_1 - \nu(\sigma_2 + \sigma_3)]. \tag{13}$$

According to Equation (13), Equation (11) can be expressed as:

$$\begin{cases} \sigma_1^* = \frac{\sigma_1}{(1 - \beta D)} = \frac{\sigma_1 E \varepsilon_1}{\sigma_1 - \nu(\sigma_2 + \sigma_3)}, \\ \sigma_2^* = \frac{\sigma_2}{(1 - \beta D)} = \frac{\sigma_2 E \varepsilon_1}{\sigma_1 - \nu(\sigma_2 + \sigma_3)}, \\ \sigma_3^* = \frac{\sigma_3}{(1 - \beta D)} = \frac{\sigma_3 E \varepsilon_1}{\sigma_1 - \nu(\sigma_2 + \sigma_3)}. \end{cases} \quad (14)$$

Substitution of Equation (14) into Equation (7) yields the expressions for I_1 and J_2 as:

$$\begin{cases} I_1 = \sigma_1^* + \sigma_2^* + \sigma_3^* = \frac{E \varepsilon_1 (\sigma_1 + \sigma_2 + \sigma_3)}{\sigma_1 - \nu(\sigma_2 + \sigma_3)}, \\ J_2 = \frac{1}{6} \left\{ \frac{E^2 \varepsilon_1^2 [(\sigma_1 - \sigma_2)^2 + (\sigma_2 - \sigma_3)^2 + (\sigma_3 - \sigma_1)^2]}{[\sigma_1 - \nu(\sigma_2 + \sigma_3)]^2} \right\}. \end{cases} \quad (15)$$

In the uniaxial compression test, $\sigma_2 = \sigma_3 = 0$, then $I_1 = E\varepsilon$, $J_2 = \frac{1}{3}E^2\varepsilon^2$, so that the damage body of the load damage variable D_σ is obtained as follows:

$$D_\sigma = \begin{cases} 0, \varepsilon < \varepsilon_c, \\ 1 - \exp \left[- \left(\frac{\alpha E \varepsilon + \frac{1}{\sqrt{3}} E \varepsilon - C}{K} \right)^m \right], \varepsilon \geq \varepsilon_c. \end{cases} \quad (16)$$

Therefore, when the axial stress exceeds C , the damage constitutive model of the damaged body is obtained as:

$$\sigma_c = E\varepsilon \left\{ 1 - \beta + \beta \exp \left[- \left(\frac{\alpha E \varepsilon + \frac{1}{\sqrt{3}} E \varepsilon - C}{K} \right)^m \right] \right\}. \quad (17)$$

In this study, the Kelvin body is parallel with the damaged body, and for the Kelvin body we obtain:

$$\begin{cases} \sigma_k = \sigma_a + \sigma_b, \\ \sigma_a = k_a \varepsilon_a, \\ \sigma_b = \eta \dot{\varepsilon}_b. \end{cases} \quad (18)$$

In the combinatorial model, the parallel relationship leads to:

$$\begin{cases} \sigma = \sigma_k + \sigma_c, \\ \varepsilon = \varepsilon_k = \varepsilon_a = \varepsilon_b. \end{cases} \quad (19)$$

Since the uniaxial compressive stress–strain curve crosses the origin of the coordinate system, when $\varepsilon < \varepsilon_c$, the stress–strain function is assumed to be $\sigma = A\varepsilon^2 + B\varepsilon$. Meanwhile, by substituting Equations (17) and (18) into Equation (19), the damage constitutive model under the normal temperature loading of Beishan granite can be expressed as follows:

$$\sigma = \begin{cases} A\varepsilon^2 + B\varepsilon, \varepsilon < \varepsilon_c, \\ k_a \varepsilon + \eta \dot{\varepsilon} + E\varepsilon \left\{ 1 - \beta + \beta \exp \left[- \left(\frac{\alpha E \varepsilon + \frac{1}{\sqrt{3}} E \varepsilon - C}{K} \right)^m \right] \right\}, \varepsilon \geq \varepsilon_c. \end{cases} \quad (20)$$

3.2. High-Temperature Damage Constitutive Model

It is observed from Figure 8b, that the uniaxial compressive strength and the modulus of elasticity gradually decrease with increasing temperature, and the thermal damage variable D_T is defined as:

$$D_T = 1 - \frac{E_T}{E_0}, \tag{21}$$

where E_T and E_0 are the modulus of elasticity after heat treatment and at 25 °C, respectively.

Temperature affects the parameters K and m of the Weibull distribution [52], assuming that the parameters are:

$$\begin{cases} K(T) = K_0(1 - D_T), \\ m(T) = m_0(1 - D_T). \end{cases} \tag{22}$$

Meanwhile, the viscosity η and the angle of internal friction φ are bound to vary with temperature [53–55]. Substituting Equations (21) and (22) into Substituting Equation (20), the constitutive equation of the thermally damaged Beishan granite is obtained as:

$$\sigma_T = \begin{cases} A\varepsilon^2 + B\varepsilon, \varepsilon < \varepsilon_c, \\ k_a\varepsilon(1 - D_T) + \eta_T\dot{\varepsilon} + E_T\varepsilon \left\{ 1 - \beta + \beta \exp \left[- \left(\frac{\alpha_T E_T \varepsilon + \frac{1}{\sqrt{3}} E_T \varepsilon - C}{K(T)} \right)^{m(T)} \right] \right\}, \varepsilon \geq \varepsilon_c. \end{cases} \tag{23}$$

where $\alpha_T = \frac{\sin \varphi_T}{\sqrt{9+3(\sin \varphi_T)^2}}$. And $\varphi_T, E_T,$ and η_T are the internal friction angle, the elastic modulus, and the viscosity coefficient, respectively, at different temperatures.

4. Solution of Constitutive Equation

The proposed constitutive equation of thermally damaged Beishan granite is relatively complex and involves several parameters. Based on the threshold point and peak point of the uniaxial compressive stress–strain curve, some of the parameters can be determined. The viscosity coefficient η_T and internal friction angle φ_T can be determined by referring to the relevant experimental results.

4.1. K and m

According to the constitutive equation, when $\varepsilon \geq \varepsilon_c$, the following equation can be obtained at the peak point $(\varepsilon_D, \sigma_D)$.

$$\sigma_D = k_a\varepsilon_D(1 - D_T) + \eta_T\dot{\varepsilon}_D + E_T\varepsilon_D \left\{ 1 - \beta + \beta \exp \left[- \left(\frac{\alpha_T E_T \varepsilon_D + \frac{1}{\sqrt{3}} E_T \varepsilon_D - C}{K(T)} \right)^{m(T)} \right] \right\} \tag{24}$$

Additionally, the peak point satisfies $\frac{\partial \sigma}{\partial \varepsilon} \Big|_{\substack{\sigma=\sigma_D \\ \varepsilon=\varepsilon_D}} = 0$, so that:

$$\begin{aligned} \frac{\partial \sigma}{\partial \varepsilon} \Big|_{\substack{\sigma=\sigma_D \\ \varepsilon=\varepsilon_D}} &= k_a(1 - D_T) + E_T \left\{ 1 - \beta + \beta \exp \left[- \left(\frac{\alpha_T E_T \varepsilon_D + \frac{1}{\sqrt{3}} E_T \varepsilon_D - C}{K(T)} \right)^{m(T)} \right] \right\} - \\ &E_T \varepsilon_D \beta \exp \left[- \left(\frac{\alpha_T E_T \varepsilon_D + \frac{1}{\sqrt{3}} E_T \varepsilon_D - C}{K(T)} \right)^{m(T)} \right] \cdot m(T) \left(\frac{\alpha_T E_T \varepsilon_D + \frac{1}{\sqrt{3}} E_T \varepsilon_D - C}{K(T)} \right)^{m(T)-1} \\ &\cdot \frac{\alpha_T E_T + \frac{1}{\sqrt{3}} E_T}{K(T)} = 0 \end{aligned} \tag{25}$$

The values of K and m at different temperatures can be obtained using Equations (24) and (25) at different temperatures.

4.2. A and B

A and B are the fitted coefficients of the quadratic function, and since the function is continuous at the segment point, the threshold point (ϵ_C, C) satisfies:

$$A\epsilon_C^2 + B\epsilon_C = k_a\epsilon_C(1 - D_T) + \eta_T \dot{\epsilon}_C + E_T\epsilon_C \left\{ 1 - \beta + \beta \exp \left[- \left(\frac{\alpha_T E_T \epsilon_C + \frac{1}{\sqrt{3}} E_T \epsilon_C - C}{K(T)} \right)^{m(T)} \right] \right\} \tag{26}$$

$$\left. \frac{\partial \sigma}{\partial \epsilon} \right|_{\substack{\sigma = C \\ \epsilon = \epsilon_C}} = k_a(1 - D_T) + E_T \left\{ 1 - \beta + \beta \exp \left[- \left(\frac{\alpha_T E_T \epsilon_C + \frac{1}{\sqrt{3}} E_T \epsilon_C - C}{K(T)} \right)^{m(T)} \right] \right\} - E_T \epsilon_C \beta \exp \left[- \left(\frac{\alpha_T E_T \epsilon_C + \frac{1}{\sqrt{3}} E_T \epsilon_C - C}{K(T)} \right)^{m(T)} \right] \cdot m(T) \left(\frac{\alpha_T E_T \epsilon_C + \frac{1}{\sqrt{3}} E_T \epsilon_C - C}{K(T)} \right)^{m(T)-1} \tag{27}$$

$$\frac{\alpha_T E_T + \frac{1}{\sqrt{3}} E_T}{K(T)} = 2A\epsilon_C + B$$

The values of A and B at different temperatures can be obtained using Equations (26) and (27).

5. The Evolution of Thermal Damage in Beishan Granites

To verify the applicability of the model of the thermally damaged Beishan granite, uniaxial compression tests were conducted on Beishan granite following treatment at different temperatures (25 °C, 200 °C, 400 °C, 600 °C and 800 °C). The results are shown in Table 1.

Table 1. Parameters of the uniaxial compression experiment on Beishan granite with different temperature treatments.

T/ °C	E/GPa	σ_D /MPa	ϵ_D	C/MPa	ϵ_C	η	φ
25	14,051.58	111.8710	0.00882	44.7484	0.00376	2.8669	47.36
200	10,290.00	79.4000	0.00995	31.7600	0.00417	1.5620	52.86
400	9322.24	68.1520	0.01122	27.2608	0.00572	1.1271	52.20
600	7280.79	52.3744	0.01109	20.9498	0.00651	0.8726	53.29
800	2402.92	30.5807	0.02031	12.2323	0.01252	0.6921	50.87

The model was validated by comparison to the above-mentioned solution and by uniaxial compression experimental results. Through multiple fitting tests, the damage correction coefficient β was determined to be 0.9, and the values of the relevant parameters are presented in Table 2. Figure 10 shows the comparison between the theoretical and the experimental values.

Table 2. Parameters of the constitutive model of thermally damage granite.

T/ °C	D_T	K	m	A	B
25	0.00000	38.1773	2.709271	1,490,249.16	6318.17
200	0.26770	75.7117	2.328035	1,045,909.61	5939.64
400	0.33657	94.5893	1.671817	337,823.69	6882.43
600	0.48185	47.8525	1.380419	140,391.48	5815.79
800	0.82899	37.5851	1.484007	17,505.03	1881.04

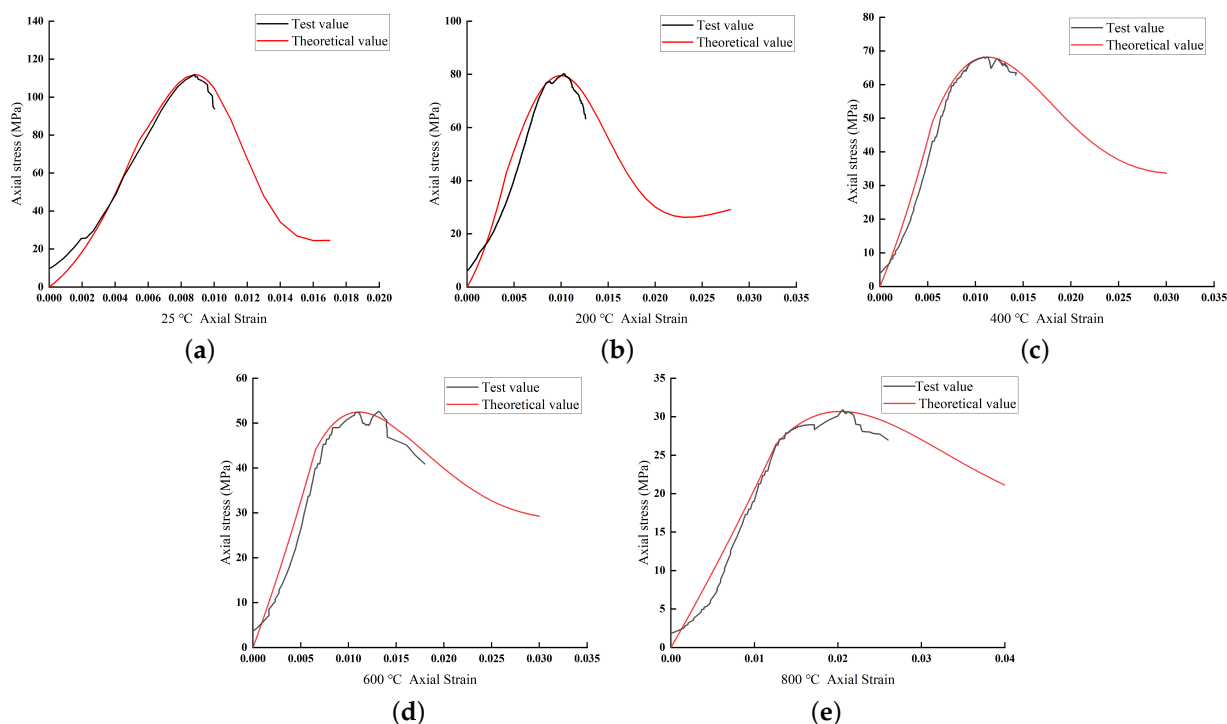


Figure 10. Comparison between the theoretical value and the experimental value. (a) $T = 25\text{ }^{\circ}\text{C}$; (b) $T = 200\text{ }^{\circ}\text{C}$; (c) $T = 400\text{ }^{\circ}\text{C}$; (d) $T = 600\text{ }^{\circ}\text{C}$; (e) $T = 800\text{ }^{\circ}\text{C}$.

It is observed from Figure 10 that as the temperature rises, the theoretical values are greater than the experimental values except for the peak point and its nearby points. The main reasons for this are as follows: first, the theoretical derivation assumes the ideal state. Second, the microelement strength criterion of rock is the D–P criterion, and the calculated damage strength is usually high [56]. However, the correction in this study is desirable and should be further adjusted based on experimental results to make it closer to the actual situation. Third, in the thermal damage analysis, the temperature only causes damage to accommodate several rock microelements, but in fact, the strength of other microelements will also be influenced and then affect the strength and stability of the rock. Overall, this study optimizes the mechanical model and criterion and has certain applicability and research significance.

6. PFC-Based High-Temperature Damage Simulation

Particle flow code (PFC) is one of the most important tools for investigations of the mechanical properties of rocks [57]. PFC uses particles as the basic unit to study the complex deformation properties of materials. It treats the material as a collection of tiny spherical or disc particles, which are connected to each other by “adhesions”. The mechanical properties are determined by both the physical and mechanical properties of the particles and the contact. The advantage of PFC is that it can simulate the material transport and stress transfer inside the specimen, as well as the crack opening, extension, and elongation processes. It can monitor the location and number of microcracks generated during the damage of the specimen, the stress-strain state, the morphology of the crack when it penetrates, and the strength of the specimen. Therefore, it can simulate the mechanical properties of materials at the microscopic scale. In this study, PFC^{2D} was applied to simulate the high-temperature damage of Beishan granite. The simulation process was divided into four steps: sample formation, heat treatment, prepressure, and loading. The flow chart of the modeling is shown in Figure 11.

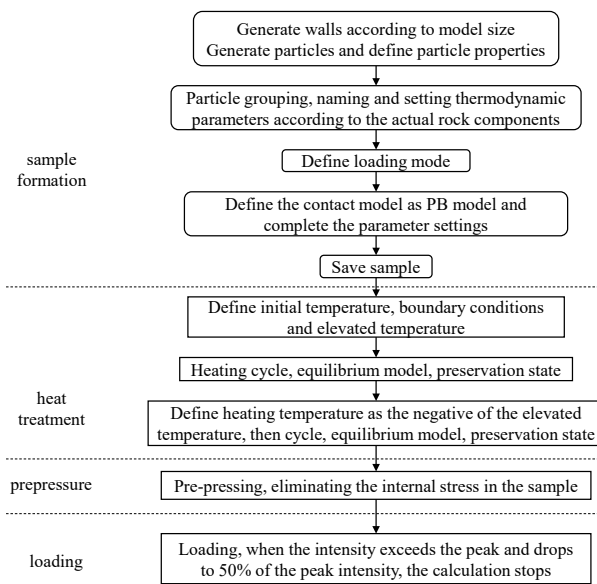


Figure 11. Flow chart of PFC simulation.

First, the model was generated using the FISH function of PFC^{2D}. An outer wall with a height of 100 mm and width of 50 mm was built and filled with particles. The minimum particle size was 0.6 mm, and the ratio of the maximum particle size to the minimum particle size was 1.66. A total of 9017 particles were filled, and the initial establishment of the model was completed after equilibrating the system. Considering that the components of Beishan granite are 67.90% feldspar, 27.40% quartz, and 4.70% mica, 6123 particles were randomly selected and designated as the feldspar group. Similarly, 2471 particles were in the quartz group, and 423 particles were in the mica group. Figure 12 describes the generated particle flow model.

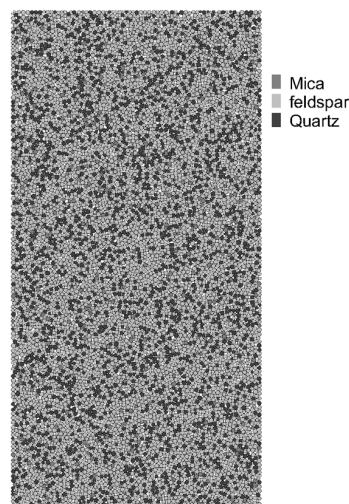


Figure 12. Particle flow model of Beishan granite.

Since the parallel bonding model has successfully reproduced the mechanical behavior of rock [58], it was chosen as the interparticle cementation model in this study. When calibrating the related parameters, the PFC^{2D} manual recommends using the trial-and-error method to obtain simulation results that are consistent with the experimental results [59]. After trial calculations and simulation tests, the parameters of the particle and the contact were determined and are shown in Table 3. Following the parameter calibration, the thermal microparameters of the granite minerals were defined and are shown in Table 4.

Table 3. Parameters of the particle and the contact.

Category	Parameter	Unit	Value
Particle	Minimum particle size	m	6×10^{-4}
	Max/min particle size ratio	-	1.66
	Density	kg/cm ³	2.564
	Elastic modulus	Pa	1.4×10^{10}
	Friction coefficient	-	0.5
	Stiffness ratio	-	1
Contact	Bonding tensile strength	Pa	1×10^8
	Gluing adhesion	Pa	1×10^8
	Gluing friction angle	°	47.36
	Friction coefficient	-	0.5
	Radius multiplier	-	1
	Normal to tangential stiffness ratio	-	1
	Stiffness ratio	-	1

Table 4. Thermal microparameters of granite minerals.

Mineral	Linear Coefficient of Thermal Expansion / $10 \times 10^{-6} \cdot \text{C}^{-1}$	Thermal Conductivity / $\text{W} \cdot \text{Mk}^{-1}$	Specific Heat Capacity / $\text{J} \cdot \text{kg}^{-1} \cdot \text{C}^{-1}$
Feldspar	15	2×10^{-5}	800
Quartz	10	2×10^{-5}	800
Mica	3.5	2×10^{-5}	800

Following the definition of the parameters, the model was heat-treated using the thermal module. It was set as the first module, and the force module was set as the second module because they cannot be calculated simultaneously in PFC^{2D}. The calculation modes can be modified at any time during a PFC analysis by issuing the set thermal and set mechanical commands with the on/off keywords. To perform the thermal calculation, the velocity and displacement of both the ball and the wall are specified to be zero, the initial and boundary conditions are specified, the temperature is applied to the particle with the given thermodynamic parameters, and the thermal step is executed by means of a loop command. When the particle reaches the defined temperature (200 °C, 400 °C, 600 °C and 800 °C) and reaches a steady state, the computational state is saved. Further, the specimen is cooled down to room temperature by the same operation. The distribution of thermal cracks is shown in Figure 13.

Figure 13 shows that 10 tensile cracks are produced at 200 °C. With increasing temperature, the number of cracks gradually increases. Shear cracks appear at 400 °C, and tensile cracks account for 72.93% of the total cracks. With a further increase in the temperature, the crack initiation, expansion and development accelerate, producing 7967 tensile cracks and 7704 shear cracks at 600 °C. The numbers of the two types of cracks are approximately equal. When the temperature reaches 800 °C, the thermal cracks increase rapidly and spread throughout the model, 6281 tensile cracks and 8046 shear cracks are formed, and the number of tensile cracks accounts for 42.08% of the total cracks.

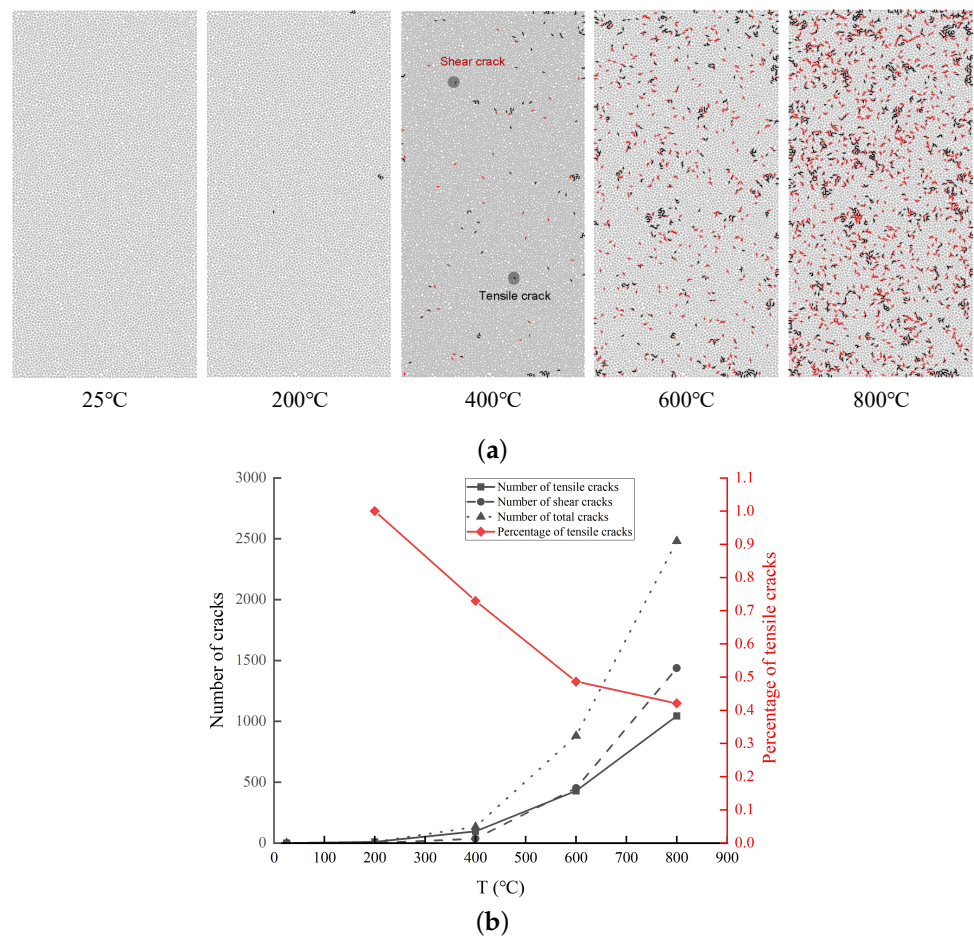


Figure 13. Thermal crack development. (a) Thermal crack distribution; (b) The number of cracks.

After the cooling step, the thermal module was closed, and the compressive stage was initiated. Considering that the prestress was generated by the particle contact in the model generation step, the model was precompressed at an axial strain rate of 0.2 s^{-1} . The uniaxial compression test was performed at the same rate after precompression. When the load reached the peak strength and then decreased 50%, the calculation stopped. Figure 14a shows the distribution of cracks after model failure.

Figure 14b shows that 829 tensile cracks and 126 shear cracks form after reaching the damage strength at $25 \text{ }^\circ\text{C}$, the tensile cracks account for 86.81% of the total number of cracks, and the damage is mainly due to tensile damage. From the appearance of the sample, the distribution of cracks is concentrated, and is mainly located in the upper part of the model, and the cracks develop from the middle of the upper surface to the middle of the left and right sides. The shear zone gradually develops into a rupture surface. With increasing temperature, the number of tensile cracks gradually increases, while the number of shear cracks increases faster, and the latter exceeds the former at $800 \text{ }^\circ\text{C}$. The trend of the total number of cracks is similar to that of shear cracks, indicating that the specimen is significantly affected by shear damage. A total of 1489 tensile cracks and 1890 shear cracks form after reaching the damage strength at $800 \text{ }^\circ\text{C}$. The shear cracks account for 55.93% of the total number of cracks, which is $15\times$ that at $25 \text{ }^\circ\text{C}$, indicating that the damage is changed from mainly tensile cracks to mainly shear cracks with increasing temperature. From the images it is observed that the cracks are more scattered at $800 \text{ }^\circ\text{C}$ than at $25 \text{ }^\circ\text{C}$; they develop from the top of the upper surface to the middle of the right side while also expanding from the middle of the left side to the lower surface, forming two rupture surfaces. A higher temperature corresponds to a higher degree of damage.

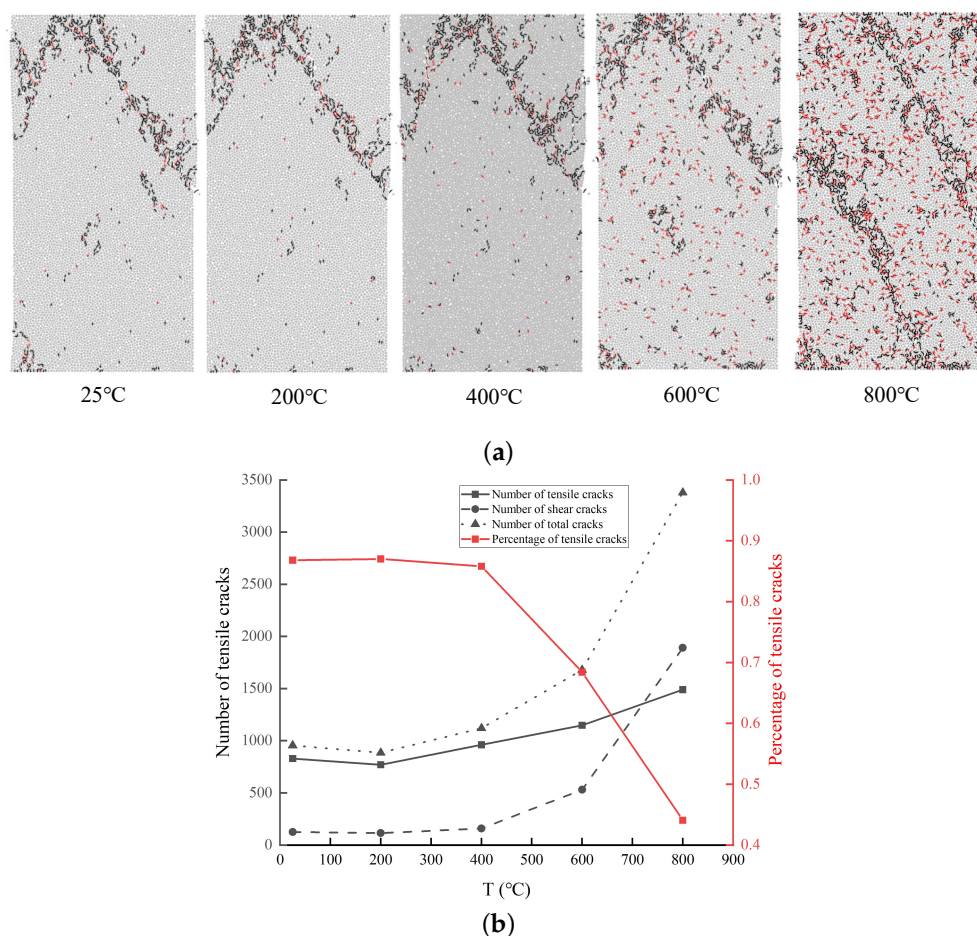


Figure 14. Crack development following uniaxial compression. (a) Distribution of crack of model failure; (b) The number of cracks.

7. Conclusions

In this study, heat treatment, NMR, uniaxial compression, and Brazilian splitting tests were carried out to construct a constitutive model of thermally damaged Beishan granite. Moreover, PFC^{2D} was used to simulate the development of fractures in heat-treated rock models under uniaxial compression. The following conclusions are obtained:

1. The mass, volume, density, wave velocity, elastic modulus, peak stress, and other experimental results of Beishan granite were obtained. They indicate that temperature has a significant effect on physical and mechanical properties. The high temperature not only gives rise to microcracks between grains but also penetration cracks when the phase change point of quartz is reached. Among these, the microcracks initiate and expand rapidly. High temperature reduces the strength and brittleness of rock.
2. The mechanical model is assumed to consist of a Kelvin body and a damaged body in parallel. Based on the damage theory, the Weibull distribution, the Lemaitre strain equivalence assumption, the damage threshold, and the residual strength, this study innovatively modified the D–P criterion and damage stress. The constitutive model of thermally damaged Beishan granite. The solution of the parameters in the constitutive model was proposed. It was found that the Weibull distribution parameters K and m have significant influences on the curve trend. The theoretical study has produced results essentially in agreement with the experimental ones. The parameters required for the model are conventional mechanical parameters that can be calculated from the uniaxial test results, thus making the model convenient to apply.
3. In fact, the variation of stress-strain curves of rocks under different treatment temperatures is complex. Since rock is non-homogeneous material, there will be certain

differences in the properties of specimens used for different temperature levels, which may cause dispersion of the experimental results. Parameters such as K , m , A , and B in the proposed constitutive model highly depend on the experimental results. Therefore, it is difficult to define temperature-dependent expressions for them. A constitutive equation that can accurately describe the stress-strain relationship of rock with temperature as the unique variable will be an important research direction. The following work will be conducted from the aspects of specimen preparation, selection, test conditions, test methods, and equation derivation.

4. According to the simulation of PFC^{2D}, there are two main types of rock cracks: shear cracks and tensile cracks. The cracks change from mainly tensile cracks to mainly shear cracks with increasing temperature. A higher temperature implies a more significant effect of shear cracking and a higher degree of damage.

Author Contributions: Conceptualization, X.Z. and M.W.; methodology, X.Z. and M.W.; software, X.Z., M.W., and Y.C.; validation, X.Z., M.W., and Y.C.; formal analysis, X.Z., M.W., and Z.L.; investigation, X.Z., M.W., and Y.C.; resources, X.Z., M.W. and Z.L.; data curation, X.Z., M.W., Z.L., and Y.C.; writing—original draft, X.Z. and M.W.; writing—review and editing, X.Z., M.W., and Z.L.; visualization, X.Z. and M.W.; supervision, X.Z., M.W., Z.L., and Y.C.; project administration, X.Z. and M.W.; funding acquisition, X.Z. and M.W. All authors have read and agreed to the published version of the manuscript.

Funding: This research was funded by the National Natural Science Foundation of China [No. 52268038], The Applied Basic Research Project of Yunnan Province [No. 202201AT070159], The 1st Professional Degree Postgraduate Practice Innovation Project of Yunnan University [No. 2021Y061].

Institutional Review Board Statement: Not applicable.

Informed Consent Statement: Not applicable.

Data Availability Statement: The data that support the findings of this study are available from the corresponding author upon reasonable request.

Acknowledgments: The authors would like to thank all of the cited authors and the anonymous reviewers in this article for their helpful suggestions.

Conflicts of Interest: The authors declare no conflict of interest.

References

1. Wang, J. Progress of Geological Disposal of High-level Radioactive Waste in China in the 21th Century. *At. Energy Sci. Technol.* **2019**, *53*, 2072–2082.
2. Wang, R.; Zhuo, Z.; Zhou, H.W.; Liu, J.F. A fractal derivative constitutive model for three stages in granite creep. *Results Phys.* **2017**, *7*, 2632–2638. <https://doi.org/10.1016/j.rinp.2017.07.051>.
3. Rechard, R.P. Historical background on performance assessment for the Waste Isolation Pilot Plant. *Reliab. Eng. Syst. Saf.* **2000**, *69*, 5–46. [https://doi.org/10.1016/S0951-8320\(00\)00023-5](https://doi.org/10.1016/S0951-8320(00)00023-5).
4. Goldstein, J. How to build a better sepulcher: Lessons from New Mexico's Waste Isolation Pilot Plant. *Bull. At. Sci.* **2011**, *67*, 77–88. <https://doi.org/10.1177/0096340211421473>.
5. Sasaki, T.; Rutqvist, J. Effects of time-dependent deformation of shale on the integrity of a geological nuclear waste repository. *Int. J. Rock Mech. Min. Sci.* **2022**, *158*, 105206. <https://doi.org/10.1016/j.ijrmms.2022.105206>.
6. Chang, K.W.; Nole, M.; Stein, E.R. Reduced-order modeling of near-field THMC coupled processes for nuclear waste repositories in shale. *Comput. Geotech.* **2021**, *138*, 104326. <https://doi.org/10.1016/j.compgeo.2021.104326>.
7. Li, L.; Shu, X.; Cheng, Y.; Wen, M.; Zhou, H.; Lu, X.; Lu, Y.; Chen, J.; Dong, F. High immobilizing capacity of natural granite as glass-ceramic matrix to simulated trivalent actinide waste. *Radiat. Phys. Chem.* **2022**, *195*, 110067. <https://doi.org/10.1016/j.radphyschem.2022.110067>.
8. Gautam, P.K.; Verma, A.K.; Singh, T.N.; Hu, W.; Singh, K.H. Experimental investigations on the thermal properties of Jalore granitic rocks for nuclear waste repository. *Thermochim. Acta* **2019**, *681*, 178381. <https://doi.org/10.1016/j.tca.2019.178381>.
9. Hudson, J.A.; Bäckström, A.; Rutqvist, J.; Jing, L.; Backers, T.; Chijimatsu, M.; Christiansson, R.; Feng, X.T.; Kobayashi, A.; Koyama, T.; et al. Characterising and modelling the excavation damaged zone in crystalline rock in the context of radioactive waste disposal. *Environ. Geol.* **2009**, *57*, 1275–1297. <https://doi.org/10.1007/s00254-008-1554-z>.

10. Tsang, C.F.; Bernier, F.; Davies, C. Geohydromechanical processes in the Excavation Damaged Zone in crystalline rock, rock salt, and indurated and plastic clays—In the context of radioactive waste disposal. *Int. J. Rock Mech. Min. Sci.* **2005**, *42*, 109–125. <https://doi.org/10.1016/j.ijrmms.2004.08.003>.
11. Rutqvist, J.; Börgesson, L.; Chijimatsu, M.; Hermelind, J.; Jing, L.; Kobayashi, A.; Nguyen, S. Modeling of damage, permeability changes and pressure responses during excavation of the TSX tunnel in granitic rock at URL, Canada. *Environ. Geol.* **2009**, *57*, 1263–1274. <https://doi.org/10.1007/s00254-008-1515-6>.
12. Cai, Y.; Liu, Y. Geometry Parameter Analysis on the Fracture Nterconnectivity of Rock Mass Surrounding Nuclear Waste Repositories. *J. Geol. Hazards Environ. Preserv.* **2001**, *33*, 39–47.
13. Laverov, N.P.; Yudinsev, S.V.; Kochkin, B.T.; Malkovsky, V.I. The Russian Strategy of using Crystalline Rock as a Repository for Nuclear Waste. *Elements* **2016**, *12*, 253–256. <https://doi.org/10.2113/gselements.12.4.253>.
14. Hadermann, J.; Heer, W. The Grimsel (Switzerland) migration experiment: integrating field experiments, laboratory investigations and modelling. *J. Contam. Hydrol.* **1996**, *21*, 87–100. [https://doi.org/10.1016/0169-7722\(95\)00035-6](https://doi.org/10.1016/0169-7722(95)00035-6).
15. Fairhurst, C. Nuclear waste disposal and rock mechanics: contributions of the Underground Research Laboratory (URL), Pinawa, Manitoba, Canada. *Int. J. Rock Mech. Min. Sci.* **2004**, *41*, 1221–1227. <https://doi.org/10.1016/j.ijrmms.2004.09.001>.
16. WNA. World Nuclear Performance Report 2022. Available online: <https://www.world-nuclear.org/world-nuclear-performance-report.aspx> (accessed on 1 November 2022).
17. Chen, L.; Wang, C.P.; Liu, J.F.; Li, Y.; Liu, J.; Wang, J. Effects of temperature and stress on the time-dependent behavior of Beishan granite. *Int. J. Rock Mech. Min. Sci.* **2017**, *93*, 316–323. <https://doi.org/10.1016/j.ijrmms.2016.11.007>.
18. Heierli, J. A comparative study of engineering options for the disposal of high-level radioactive waste with regard to thermal effects and chemical degradation. *J. Nucl. Sci. Technol.* **2016**, *53*, 1276–1295. <https://doi.org/10.1080/00223131.2015.1105163>.
19. Takarli, M.; Prince, W.; Siddique, R. Damage in granite under heating/cooling cycles and water freeze–thaw condition. *Int. J. Rock Mech. Min. Sci.* **2008**, *45*, 1164–1175. <https://doi.org/10.1016/j.ijrmms.2008.01.002>.
20. Qin, Y.; Tian, H.; Xu, N.X.; Chen, Y. Physical and Mechanical Properties of Granite After High-Temperature Treatment. *Rock Mech. Rock Eng.* **2020**, *53*, 305–322. <https://doi.org/10.1007/s00603-019-01919-0>.
21. Zhang, W.; Sun, Q.; Hao, S.; Geng, J.; Lv, C. Experimental study on the variation of physical and mechanical properties of rock after high temperature treatment. *Appl. Therm. Eng.* **2016**, *98*, 1297–1304. <https://doi.org/10.1016/j.applthermaleng.2016.01.010>.
22. Zhao, X.G.; Xu, H.R.; Zhao, Z.; Guo, Z.; Cai, M.; Wang, J. Thermal conductivity of thermally damaged Beishan granite under uniaxial compression. *Int. J. Rock Mech. Min. Sci.* **2019**, *115*, 121–136. <https://doi.org/10.1016/j.ijrmms.2019.01.014>.
23. Chen, Y.L.; Wang, S.R.; Ni, J.; Azzam, R.; Fernández-steeger, T.M. An experimental study of the mechanical properties of granite after high temperature exposure based on mineral characteristics. *Eng. Geol.* **2017**, *220*, 234–242. <https://doi.org/10.1016/j.enggeo.2017.02.010>.
24. Gautam, P.K.; Verma, A.K.; Jha, M.K.; Sharma, P.; Singh, T.N. Effect of high temperature on physical and mechanical properties of Jalore granite. *J. Appl. Geophys.* **2018**, *159*, 460–474. <https://doi.org/10.1016/j.jappgeo.2018.07.018>.
25. Tomás, R.; Cano, M.; Pulgarín, L.F.; Brotóns, V.; Benavente, D.; Miranda, T.; Vasconcelos, G. Thermal effect of high temperatures on the physical and mechanical properties of a granite used in UNESCO World Heritage sites in north Portugal. *J. Build. Eng.* **2021**, *43*, 102823. <https://doi.org/10.1016/j.jobte.2021.102823>.
26. Wu, Y.; Li, X.Z.; Huang, Z.; Xue, S. Effect of temperature on physical, mechanical and acoustic emission properties of Beishan granite, Gansu Province, China. *Nat. Hazards* **2021**, *107*, 1577–1592. <https://doi.org/10.1007/s11069-021-04647-3>.
27. Xu, X.L.; Karakus, M. A coupled thermo-mechanical damage model for granite. *Int. J. Rock Mech. Min. Sci.* **2018**, *103*, 195–204. <https://doi.org/10.1016/j.ijrmms.2018.01.030>.
28. Liu, W.; Dan, Z.; Jia, Y.; Zhu, X. On the Statistical Damage Constitutive Model and Damage Evolution of Hard Rock at High-Temperature. *Geotech. Geol. Eng.* **2020**, *38*, 4307–4318. <https://doi.org/10.1007/s10706-020-01296-4>.
29. Wang, F.; Konietzky, H. Thermo-Mechanical Properties of Granite at Elevated Temperatures and Numerical Simulation of Thermal Cracking. *Rock Mech. Rock Eng.* **2019**, *52*, 3737–3755. <https://doi.org/10.1007/s00603-019-01837-1>.
30. Wang, S.; Liao, H.; Chen, Y.; Fernández-Steeger, T.M.; Du, X.; Xiong, M.; Liao, S. Damage Evolution Constitutive Behavior of Rock in Thermo-Mechanical Coupling Processes. *Materials* **2021**, *14*, 7840. <https://doi.org/10.3390/ma14247840>.
31. Xie, S.; Han, Z.; Chen, Y.; Wang, Y.; Zhao, Y.; Lin, H. Constitutive modeling of rock materials considering the void compaction characteristics. *Arch. Civ. Mech. Eng.* **2022**, *22*, 60.
32. Zhao, F.; Sun, Q.; Zhang, W. Fractal analysis of pore structure of granite after variable thermal cycles. *Environ. Earth Sci.* **2019**, *78*, 677. <https://doi.org/10.1007/s12665-019-8703-4>.
33. Miao, S.; Pan, P.Z.; Zhao, X.; Shao, C.; Yu, P. Experimental Study on Damage and Fracture Characteristics of Beishan Granite Subjected to High-temperature Treatment with DIC and AE Techniques. *Rock Mech. Rock Eng.* **2021**, *54*, 721–743. <https://doi.org/10.1007/s00603-020-02271-4>.
34. Li, Q.; Li, X.; Yin, T. Factors affecting pore structure of granite under cyclic heating and cooling: A nuclear magnetic resonance investigation. *Geothermics* **2021**, *96*, 102198. <https://doi.org/10.1016/j.geothermics.2021.102198>.
35. Wang, F.; Konietzky, H. Thermal damage evolution of granite under slow and high-speed heating conditions. *Comput. Geotech.* **2020**, *123*, 103590. <https://doi.org/10.1016/j.compgeo.2020.103590>.
36. Liu, L.; Li, H.; Li, X.; Zhang, G.; Wu, R. Research on mechanical properties of heterogeneous rocks using grain-based model under uniaxial compression. *Chin. J. Geotech. Eng.* **2020**, *42*, 542–550.

37. Xie, S.; Han, Z.; Lin, H. A quantitative model considering crack closure effect of rock materials. *Int. J. Solids Struct.* **2022**, *251*, 111758.
38. Chen, S.; Yang, C.; Wang, G. Evolution of thermal damage and permeability of Beishan granite. *Appl. Therm. Eng.* **2017**, *110*, 1533–1542. <https://doi.org/10.1016/j.applthermaleng.2016.09.075>.
39. Sun, Q.; Hu, J. Effects of heating on some physical properties of granite, Shandong, China. *J. Appl. Geophys.* **2021**, *193*, 104410. <https://doi.org/10.1016/j.jappgeo.2021.104410>.
40. Wu, Y.; Peng, K.; Zou, Q.; Long, K.; Wang, Y. Tensile Properties and Damage Evolution Laws of Granite After High- and Low-Temperature Cycles. *Nat. Resour. Res.* **2022**, *31*, 1289–1306. <https://doi.org/10.1007/s11053-022-10025-y>.
41. Fang, W.; Jiang, H.; Li, J.; Li, W.; Li, J.; Zhao, L.; Feng, X. A new experimental methodology to investigate formation damage in clay-bearing reservoirs. *J. Pet. Sci. Eng.* **2016**, *143*, 226–234. <https://doi.org/10.1016/j.petrol.2016.02.023>.
42. Sun, Z.; Jiang, D.; Xie, K.; Wang, K.; Li, L.; Jiang, X. Thermal damage study of Beishan granite based on low field magnetic resonance. *J. China Coal Soc.* **2020**, *45*, 1081–1088. <https://doi.org/10.13225/j.cnki.jccs.2019.0164>.
43. Wu, Y.; Xi, B.; Wang, L.; Niu, X.; Wang, S.; Zhao, Y. Experimental study on physico-mechanical properties of granite after high temperature. *J. Cent. South Univ. Sci. Technol.* **2020**, *51*, 193–203.
44. Zhao, X.; Meng, W.; Zhou, L. Indentation rolling resistance based on a three-parameter Kelvin solid model. *Adv. Mech. Eng.* **2019**, *11*, 1687814019839517. <https://doi.org/10.1177/1687814019839517>.
45. Liu, Q.; Xu, X. Damage Analysis of Brittle Rock at High Temperature. *Chin. J. Rock Mech. Eng.* **2000**, pp. 408–411.
46. Wang, F.; Konietzky, H.; Herbst, M. Influence of heterogeneity on thermo-mechanical behaviour of rocks. *Comput. Geotech.* **2019**, *116*, 103184. <https://doi.org/10.1016/j.compgeo.2019.103184>.
47. Jiang, H.; Jiang, A.; Yang, X. Statistical damage constitutive model of high temperature rock based on Weibull distribution and its verification. *Rock Soil Mech.* **2021**, *42*, 1894–1902. <https://doi.org/10.16285/j.rsm.2020.1461>.
48. Martin, C.D.; Chandler, N.A. The progressive fracture of Lac du Bonnet granite. *Int. J. Rock Mech. Min. Sci. Geomech. Abstr.* **1994**, *31*, 643–659. [https://doi.org/10.1016/0148-9062\(94\)90005-1](https://doi.org/10.1016/0148-9062(94)90005-1).
49. Cao, W.; Zhao, H.; Zhang, Y.; Zhang, L. Strain softening and hardening damage constitutive model for rock considering effect of volume change and its parameters determination method. *Rock Soil Mech.* **2011**, *32*, 647–654.
50. Lemaitre, J.; Sermage, J.; Desmorat, R. A two scale damage concept applied to fatigue. *Int. J. Fract.* **1999**, *97*, 67. <https://doi.org/10.1023/A:1018641414428>.
51. Cao, R.; He, S.; Wei, J.; Wang, F. Study of modified statistical damage softening constitutive model for rock considering residual strength. *Rock Soil Mech.* **2013**, *34*, 1652–1660+1667. <https://doi.org/10.16285/j.rsm.2013.06.018>.
52. Li, T.; Gao, M.; Chen, G.; Ma, C.; Xu, Z.; Yin, H.; Chen, C.; Men, L. A thermal-mechanical-damage constitutive model for hard brittle rocks and its preliminary application. *Chin. J. Geotech. Eng.* **2017**, *39*, 1477–1484.
53. Wang, C.; Chen, L.; Liang, J.; Liu, J.; Liu, Y.; Liu, J.; Wang, J.; Zhou, H. Creep constitutive model for full creep process of granite considering thermal effect. *Rock Soil Mech.* **2014**, *35*, 2493–2500+2506. <https://doi.org/10.16285/j.rsm.2014.09.005>.
54. Zhu, Z.; Jiang, G.; Tian, H.; Wu, W.; Liang, R.; Dou, B. Study on statistical thermal damage constitutive model of rock based on normal distribution. *J. Cent. South Univ. Sci. Technol.* **2019**, *50*, 1411–1418.
55. Xi, B.; Zhao, Y.; Wan, Z.; Zhao, J.; Wang, Y. Study of Constitutive Equation of Granite Rheological Model with Thermo-Mechanical Coupling Effects. *Chin. J. Rock Mech. Eng.* **2009**, *28*, 956–967.
56. Xu, W.; Zhao, G.; Meng, X.; Cheng, X. Modified D–P criterion based on the double-fold reduction method of the true triaxial single-side unloading strength. *Chin. J. Rock Mech. Eng.* **2018**, *37*, 1813–1822. <https://doi.org/10.13722/j.cnki.jrme.2018.0135>.
57. Chen, P.; Kong, Y.; Yu, H. Research on the Calibration Method of Microparameters of a Uniaxial Compression PFC2D Model for Rock. *Chin. J. Undergr. Space Eng.* **2018**, *14*, 1240–1249.
58. Huang, Y.H.; Yang, S.Q.; Ranjith, P.G.; Zhao, J. Strength failure behavior and crack evolution mechanism of granite containing pre-existing non-coplanar holes: Experimental study and particle flow modeling. *Comput. Geotech.* **2017**, *88*, 182–198. <https://doi.org/10.1016/j.compgeo.2017.03.015>.
59. Liu, X.; Li, D.; Wang, Z.; Zhang, L. The effect of dry-wet cycles with acidic wetting fluid on strength deterioration of shaly sandstone. *Chin. J. Rock Mech. Eng.* **2016**, *35*, 1543–1554. <https://doi.org/10.13722/j.cnki.jrme.2015.1419>.